Fuel 323 (2022) 124301

Contents lists available at ScienceDirect

Fuel

journal homepage: www.elsevier.com/locate/fuel

Ni-Phosphide catalysts as versatile systems for gas-phase CO_2 conversion: Impact of the support and evidences of structure-sensitivity

Q. Zhang [a,*], L. Pastor-Pérez [a,c], J.J. Villora-Pico [b], M. Joyce [a], A. Sepúlveda-Escribano [b], M.S. Duyar [a], T.R. Reina [a,c]

[a] Department of Chemical and Process Engineering, University of Surrey, Guildford GU2 7XH, United Kingdom
[b] Laboratorio de Materiales Avanzados, Departamento de Química Inorgánica, Instituto Universitario de Materiales de Alicante, Universidad de Alicante, Apartado 99, E-03080 Alicante, Spain
[c] Department of Inorganic Chemistry and Material Sciences Institute of Seville, University of Seville-CSIC, 41092, Seville, Spain

ARTICLE INFO

Keywords:
CO_2 conversion
RWGS
Methanation
Switchable Catalysts
Ni Phosphide

ABSTRACT

We report for the first time the support dependent activity and selectivity of Ni-rich nickel phosphide catalysts for CO_2 hydrogenation. New catalysts for CO_2 hydrogenation are needed to commercialise the reverse water–gas shift reaction (RWGS) which can feed captured carbon as feedstock for traditionally fossil fuel-based processes, as well as to develop flexible power-to-gas schemes that can synthesise chemicals on demand using surplus renewable energy and captured CO_2. Here we show that Ni_2P/SiO_2 is a highly selective catalyst for RWGS, producing over 80% CO in the full temperature range of 350–750 °C. This indicates a high degree of suppression of the methanation reaction by phosphide formation, as Ni catalysts are known for their high methanation activity. This is shown to not simply be a site blocking effect, but to arise from the formation of a new more active site for RWGS. When supported on Al_2O_3 or CeAl, the dominant phase of as synthesized catalysts is $Ni_{12}P_5$. These $Ni_{12}P_5$ catalysts behave very differently compared to Ni_2P/SiO_2, and show activity for methanation at low temperatures with a switchover to RWGS at higher temperatures (reaching or approaching thermodynamic equilibrium behaviour). This switchable activity is interesting for applications where flexibility in distributed chemicals production from captured CO_2 can be desirable. Both $Ni_{12}P_5/Al_2O_3$ and $Ni_{12}P_5$/CeAl show excellent stability over 100 h on stream, where they switch between methanation and RWGS reactions at 50–70% conversion. Catalysts are characterized before and after reactions via X-ray Diffraction (XRD), X-ray Photoelectron Spectroscopy (XPS), temperature-programmed reduction and oxidation (TPR, TPO), Transmission Electron Microscopy (TEM), and BET surface area measurement. After reaction, Ni_2P/SiO_2 shows the emergence of a crystalline $Ni_{12}P_5$ phase while $Ni_{12}P_5/Al_2O_3$ and $Ni_{12}P_5$/CeAl both show the crystalline Ni_3P phase. While stable activity of the latter catalysts is demonstrated via extended testing, this Ni enrichment in all phosphide catalysts shows the dynamic nature of the catalysts during operation. Moreover, it demonstrates that both the support and the phosphide phase play a key role in determining selectivity towards CO or CH_4.

1. Introduction

Global warming caused by the accumulation of atmospheric CO_2 is considered as one of the greatest environmental threats in the 21st century [1,2]. Climate change is causing rise in sea levels, increasing the occurrence of hurricanes, wildfires, tornadoes, and floods, and having pronounced impacts on human health [3,4]. Since the consequences have the potential to bring serious unrest in the world, CO_2 utilization in the context of a circular economy has become a top priority in recent years. Among the CO_2 utilization strategies, the CO_2 methanation reaction (*eq. (1)*) and reverse water–gas shift (RWGS) reaction (*eq. (2)*) have been studied extensively [5,6,7,8] because their products (methane and carbon monoxide) can be used as fuel, in attempts at closing the combustion-based carbon cycle. Carbon monoxide (CO) from RWGS can be mixed with hydrogen (H_2), and this mixture is called synthesis gas (syngas). Syngas is used in the chemical industry as reactant to form methanol or liquid hydrocarbons.

$$CO_2 + 4H_2 \leftrightarrow CH_4 + 2H_2O \Delta H^0_{298} = -165 \cdot kJ/mol \quad (1)$$

* Corresponding author.
E-mail address: qz00288@surrey.ac.uk (Q. Zhang).

https://doi.org/10.1016/j.fuel.2022.124301
Received 4 January 2022; Received in revised form 6 April 2022; Accepted 19 April 2022
Available online 5 May 2022

$$CO_2 + H_2 \leftrightarrow CO + H_2O \Delta H^0_{298} = 41 \cdot kJ/mol \quad (2)$$

The CO_2 methanation process, also called the Sabatier reaction, is an important catalytic reaction that is of interest for renewable energy storage applications based on power-to-gas (PtG) conversion schemes. This PtG approach begins with H_2 production by water electrolysis using renewable electricity, followed by H_2 conversion with an external (captured) CO_2 source, methane being the main product. On the other hand, the reverse water − gas shift reaction coupled to chemical looping cycles (RWGS − CL) for the intensified conversion of CO_2 is regarded as a highly effective utilisation route with promising potential in industrial applications [5]. Such a hybrid process is a combination of water electrolysis with RWGS reaction. Herein, water produced in the RWGS can be recycled to the water electrolysis part, and the combination of CO and additional H_2 can be used for liquid fuel production via FT or methanol synthesis. Fig. 1 depicts a switchable process, which we have investigated in recent years [7]. The switchable nature of the process ensures flexibility in CO_2 utilisation to be able to match the demand for chemicals with surplus electricity production. For example, methane can be used as heating fuel, which has a seasonal demand change (due to residential use) and the ability to produce syngas opens up possibilities in expansion of the role of captured CO_2 in the chemical industry. Clearly the success of both routes relies on the availability of green hydrogen from renewable sources (i.e. solar or wind) [6]. In order to manage the variable production of wind and solar energy, CO_2 is captured using mature carbon capture technologies, and then utilised at times of low electricity demand to ensure renewable power conversion into chemical energy and added value products [9].

As shown in *eq. (1)* and *eq. (2)*, the CO_2 methanation is exothermic and the rWGS reaction is endothermic. The end product selectivity can be controlled by adjusting the reaction temperature and utilizing a suitable catalyst [7]. Since the RWGS reaction is favoured at high temperatures due to the endothermic nature of the reaction, a great deal of heat input is needed to produce CO. CO_2 methanation on the other hand is a highly exothermic process, which requires heat input to overcome kinetic barriers of the reaction [8]. Assuming that the designed catalyst is both active and selective to CO_2 methanation in the lower temperature range (between 300 °C and 500 °C) and RWGS in the higher temperature window (550 °C to 750 °C), the integration proposal depicted in Fig. 1 can be potentially achieved, and the desired product composition can be controlled by adjusting the reaction temperature. Under these premises, a switchable catalyst is needed.

When seeking novel switchable catalyst formulations, Ni catalysts are commonly used for both RWGS and CO_2 methanation [10,11,12]. Nickel phosphide (Ni_2P) has shown a promising catalytic performance for the dry reforming of methane (DRM) in both theoretical studies [13] and experimental research [14]. Previously, Ni_2P has also shown to be active for the hydrodeoxygenation of guaiacol [15,16]. The extraordinary hydrogen dissociation and hydrogenation abilities shown by Ni_2P has prompted us to investigate this catalyst for CO_2 hydrogenation reactions, such as the RWGS reaction and CO_2 methanation. As an additional advantage, Ni_2P has previously shown some prevention of carbon deposition in DRM [13], which is a common deactivation mechanism in some CO_2 conversion reactions.

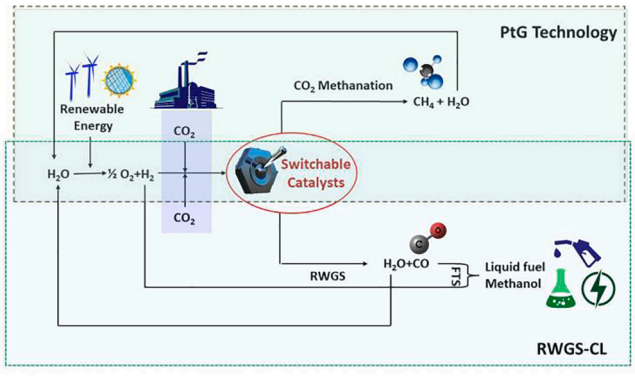

Fig. 1. Simplified scheme of the methanation and RWGS processes integrated with water electrolysis.

Since highly effective catalysts are normally composed of well isolated and dispersed active phases supported on carrier materials, supports should be chosen in conjunction with nickel phosphide phases. Various supports have been used for both CO_2 methanation and RWGS, such as SiO_2 [17], Al_2O_3 [18,19], CeO_2 [20] and CeAl mixed oxides [21]. In this regard, SiO_2 has been proven to inhibit agglomeration of metal crystals leading to enhanced CO_2 conversion levels in hydrogenation reactions [22]. Al_2O_3 is also a widely investigated support that favours high metallic dispersion, resulting in active and stable supported metal hydrogenation catalysts [23]. However, coking and sintering were promoted by the inherent acidity of Al_2O_3 during the reaction, what leads to catalyst deactivation [24]. As previously reported, the addition of ceria to alumina-based supports decreases the overall acidity thus helping to avoid carbon deposition [21].

Under this scenario, a series of nickel phosphides supported on SiO_2, Al_2O_3 or CeAl catalysts have been prepared in this work. The catalytic performances of the synthesized catalysts have been tested for both the CO_2 methanation and the RWGS reaction, targeting a switchable scheme allowing end-product flexibility. The physico-chemical properties of these catalysts have been explored, and the main reasons for their versatile behaviour are carefully addressed.

2. Experimental section

2.1. Catalysts preparation

Catalysts were synthesised using a wet impregnation method. According to previous research [25], moderately excess P content has a positive effect on stability because the excess P content is lost during the reduction process. Hence, a larger P:Ni ratio than the target stoichiometric ratio (1:2) was chosen in this synthesis. Nickel nitrate hexahydrate [$Ni(NO_3)_2{\cdot}6H_2O$] (Merck) and diammonium hydrogen phosphate [$(NH_4)_2HPO_4$] (Merck) were mixed to obtain a P:Ni ratio of 2.4:2. This mixture was dissolved in deionised water and added to the point of incipient wetness of the supports to achieve a loading of 15 wt%. The solids were then left to dry for 12 h at 80 °C and calcined at 500 °C for 2 h in air. The prepared materials were then reduced under the atmosphere of H_2 (60 mL/min) using a temperature-programmed reduction (TPR) protocol described as follows: the temperature was increased from room temperature to 650 °C at a rate of 2 °C/min, and held at 650 °C for 2 h. After cooling to room temperature in N_2, the solids were passivated in 2.1% O_2/N_2 for 12 h under the mixture of 5 mL/min of air and 45 mL/min of N_2. The same synthesis method was used for each of the three selected supports: Silica (SiO_2, SASOL), γ-Al_2O_3 (PURALOX SCFa-230, SASOL) and CeO_2-Al_2O_3 (PURALOX SCFa-160/Ce20, 80% Al_2O_3 + 20% CeO_2, SASOL).

The catalysts prepared with different supports are referred to in this manuscript as Ni_2P-SiO_2, $Ni_{12}P_5$-CeAl and $Ni_{12}P_5$-Al_2O_3 respectively, where the dominant phase identified by X-ray diffraction after synthesis was used in the name of each supported Ni_xP catalyst.

2.2. Catalysts characterization

X-ray photoelectron spectroscopy (XPS, K-ALPHA, Thermo Scientific) was used to detect the surface chemical valence states of the synthesized materials. The samples were exposed to air prior to analysis. A Al-K radiation (1486.6 eV), monochromatized by a twin crystal monochromator was used for the spectra collection, yielding a focused X-ray spot at 3 mA × 12 kV. The alpha hemispherical analyser was operated in the constant energy mode. The whole energy band was measured by

200 eV survey scan pass energies. 50 eV in a narrow scan was selectively used for some particular elements. Avantage software was used for XPS data analysis. The C 1 s core level located at 284.6 eV was used as reference binding energy. The experimental backgrounds were corrected by smart background function and surface elemental composition measures were carried out by calculating background-subtracted peak areas. The system flood gun that provides low energy electrons and low energy argon ions from a single source was used to achieve charge compensation.

X-Ray Diffraction (XRD) analysis was performed with an X'Pert Pro PANalytical using Cu-K° (40 mA, 45 kV) over a 2 theta range of 10°-80° at room temperature.

The N_2 adsorption studies at − 196 °C with an AUTOSORB-6 equipment (QUANTACHROME INSTRUMENTS) were conducted to determine the Brunauer–Emmett–Teller (BET) specific surface area. Samples were previously out-gassed at 250 °C for 4 h under vacuum. The Barret–Joyner–Halenda (BJH) method was used to estimate the average pore size and pore volume. The result has been presented in the Support Information (SI).

The hydrogen consumption of the catalyst precursors was determined by H_2-Temperature programmed reduction (TPR) in this work. The experiment was conducted in a vertical fixed bed quartz reactor under the mixture of 5 mL/min H_2 and 20 mL/min Ar. The right amount of quartz wool was placed into the reactor and 50 mg of catalyst precursor was loaded on the quartz wool, and then heated up to 920 °C at a ramp of 10 °C/min. The hydrogen consumption and water production were recorded by an online mass spectrometer (Pfeiffer, OmniStar GSD 301).

Temperature-programmed oxidation (TPO) experiments were carried out in the reactor coupled to an online mass spectrometer (Pfeiffer, OmniStar GSD 301) to measure the amount of carbon deposited on the tested catalysts. 3% O_2 in He (40 mL/min) was flowed through the sample while the temperature was increased from room temperature to 920 °C at 10 °C/min. Mass 44 (CO_2) was recorded, hence the TPO peak area could be converted to the amount of carbon deposition due to the calibrated CO_2 signal.

Thermogravimetric analysis (TGA) was conducted on the post reaction catalysts in an SDT Q600 V8.3 Instrument from TA Instruments. A flow of 100 mL/min of air was used, while the temperature was increased from room temperature to 900 °C at 10 °C/min.

2.3. Catalytic behaviour

The RWGS reactions were carried out and recorded in a vertical continuous fixed bed reactor coupled to an ABB AO2020 Advanced Optima Process Gas Analyser. The reactor was a 7 mm inner diameter quartz tube in which 0.25 g of catalyst was placed on the quartz wool in the middle of the reactor. The sample was heated in flowing N_2 from room temperature to 300 °C. Then, the N_2 was replaced by the feed gas mixture of H_2:CO_2 = 4:1 at a constant weight-hourly space velocity (WHSV) of 12000 mL/(g·h) and the products of the reaction were evaluated from 300 to 750 °C. At each temperature, the gas products were analysed after 20 min of steady-state reaction. Stability tests were conducted at a WHSV of 12000 mL/(g·h) with a H_2:CO_2 ratio of 4:1 at 450 °C for 60 h.

CO_2 conversion (*Eq. (3)*), CO selectivity (*Eq. (4)*) and CH_4 selectivity (*Eq. (5)*) could be measured based on the above tests. The relative experimental error in CO_2 conversion and CO/CH_4 selectivity in this work was given within ± 0.5 %[6]. Where n_{CO_2in} is the initial molar flow (kmol/min) of CO_2 in the reactant mixture and$n_{COout}, n_{CH_4out}, n_{CO_2out}$are the outlet molar flows in the product stream of CO, CH_4 and CO_2 respectively.

$$CO_2conversion(\%) = \frac{n_{CO_2in} - n_{CO_2out}}{n_{CO_2in}} \cdot 100 \quad (3)$$

$$COconversion(\%) = \frac{n_{COout}}{n_{CO_2in} - n_{CO_2out}} \cdot 100 \quad (4)$$

$$CH_4conversion(\%) = \frac{n_{CH_4out}}{n_{CO_2in} - n_{CO_2out}} \cdot 100 \quad (5)$$

$$COyield(\%) = \frac{n_{COout}}{n_{CO_2in}} \cdot 100 \quad (6)$$

3. Results and discussion

3.1. Characterisation of as synthesised catalysts

3.1.1. XRD analysis

Fig. 2 displays the XRD pattern of the fresh nickel phosphide catalysts. For the Ni_2P-SiO_2 catalyst, the diffraction peaks at 40.8°, 44.6°, 47.3°, 54.2°, 54.9° and 74.8° are ascribed to Ni_2P (JCPDS No. 03–0953) [26,27]. The broad scattering maximum centred at 22.5° corresponds to amorphous SiO_2 [28,29]. For the $Ni_{12}P_5$-Al_2O_3 and $Ni_{12}P_5$-CeAl catalysts, all diffraction peaks labelled by blue dots should be aligned on $Ni_{12}P_5$ (JCPDS No. 22–1190) [30,31,32]. The diffraction peak at 66.8° and the broad peak around 46° are assigned to γ-Al_2O_3 (JCPDS No. 29–0063) [31]. In addition, the peak at 2θ = 28.65° in the $Ni_{12}P_5$-CeAl sample matches well with the cubic fluorite-type CeO_2 structure (JCPDS No. 81–0792) [33,34].

Despite the use of a high P/Ni ratio of 1.2 during synthesis, all nickel phosphide active species are metal-rich and vary depending on the selected support. For the SiO_2-supported catalyst, the dominant nickel phosphide phase is Ni_2P, and there is one small peak belonging to $Ni_{12}P_5$ that was detected. In Al_2O_3-containing catalytic formulations, $Ni_{12}P_5$ is the only nickel phosphide phase observed. According to previous research, the phases of the as-synthesized nickel phosphide nanocrystals are mainly affected by the P/Ni precursor molar ratio, heating process, and time of reaction [35,36]. Once the initial P/Ni ratio and reduction condition are selected, the resulting NiP phases depend on the support type [37]. For an inert support such as SiO_2, the Ni_2P phase was obtained from a P/Ni ratio greater than 0.8 [38,39,40]. For acidic supports such as γ-Al_2O_3, a larger P/Ni (higher than 2) was required to obtain the Ni_2P phase [38,41]. In this work, P/Ni = 1.2 precursor was used in synthesis; hence, Ni_2P was produced on SiO_2 while $Ni_{12}P_5$ were formed on γ-Al_2O_3 and CeAl. The result is accordance with previous research [42].

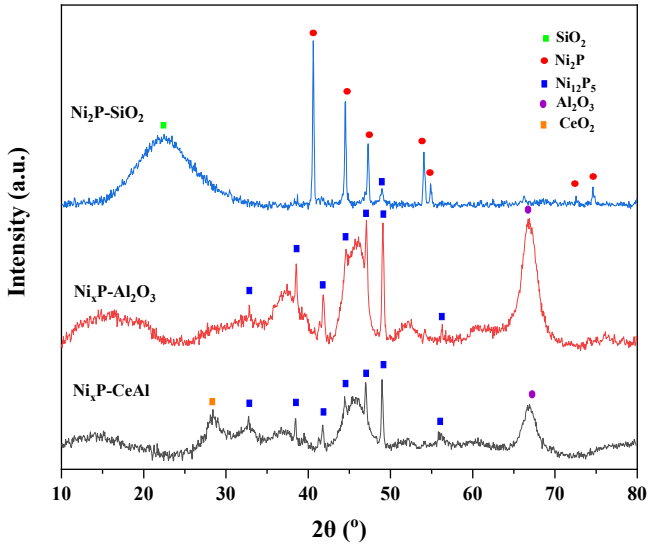

Fig. 2. X-ray diffraction patterns for fresh Ni_2P-SiO_2, $Ni_{12}P_5$-Al_2O_3 and $Ni_{12}P_5$-CeAl samples.

3.1.2. XPS study

The chemical states and coordination environment of Ni and P in the studied samples were investigated by X-ray photoelectron spectroscopy (XPS) (Fig. 3 and Table 1)., Since same chemical information was carried by two splitted Ni 2*p* spectra (Ni $2p_{1/2}$ and Ni $2p_{3/2}$), only the Ni $2p_{3/2}$ bands were curve fitted in this paper (Fig. 3 (A)). Concerning the Ni_2P-SiO_2 sample, the Ni peak at 853.9 eV was assigned to $Ni^{\delta+(0<\delta<2)}$ in Ni_2P [43]. Since the binding energy of metallic Ni vary from 852.3 to 852.9 eV in different reference, the peaks observed at 852.8 ± 0.1 eV in the $Ni_{12}P_5$-Al_2O_3 and $Ni_{12}P_5$-CeAl catalysts can be attributed to Ni in $Ni_{12}P_5$ or metallic Ni. In this case, very clear $Ni_{12}P_5$ peaks were observed in $Ni_{12}P_5$-Al_2O_3 and $Ni_{12}P_5$-CeAl samples in XRD and negatively charged $P^{\delta-}$ belongs to $Ni_{12}P_5$ was detected in the P spectra in same samples. Hence, it is reasonable to attribute the peaks located at 852.8 ± 0.1 eV to reduced $Ni^{\delta+(0<\delta<2)}$ in $Ni_{12}P_5$ phase. The magnitude of δ followed the sequence: $Ni_2P > N_{12}P_5$ [44,45,46]. Meanwhile, the presence of metallic Ni cannot be excluded. $Ni_{12}P_5$ and metallic Ni might coexistence on the surface the $Ni_{12}P_5$-Al_2O_3 and $Ni_{12}P_5$-CeAl samples. In higher binding energy region, peaks located around 856.5 eV were observed for Ni^{2+} in the passivation layer formed on the surface of studied catalysts following synthesis [43,47]. The broad peaks at 861.5 eV are attributed to the shake-up satellite peak for Ni $2p_{3/2}$ [47,48].

The P 2*p* scan is shown in Fig. 3 (B). The peaks located at 129.1 can be assigned to P belonging to nickel phosphide. The above binding energy is lower than that of elemental P (130.2 eV), indicating that the P species in nickel phosphide carries a partial negative charge ($P^{\delta-}$) [47]. Since the corresponding Ni species have a very small positive charge, the results confirm the formation of nickel phosphide, which is also in good agreement with our XRD data. Meanwhile, the peaks located around 134 eV could be ascribed to residual oxidized P species as a consequence of passivation [47,49]. It is worth noting that although the $Ni^{\delta+}$ peak was shown in the Ni 2*p* spectra of Ni_2P, there is no $P^{\delta-}$ peak belonging to Ni_2P observed in the P 2*p* spectrum of Ni_2P-SiO_2, only oxidized P species were detected. This is because of the surface oxidation; according to density functional theory (DFT) calculations, unlike nickel, phosphorus in a Ni_2P surface preferentially interacts with oxygen [50].

Compared to the alumina-containing supported catalysts, the binding energy of Ni in Ni_2P-SiO_2 is higher than that of $Ni_{12}P_5$, indicating a lower electron density and a comparatively weaker Ni-P interaction. As for the two catalysts presenting $Ni_{12}P_5$ as dominant nickel phosphide phase, the binding energy of Ni in $Ni_{12}P_5$-CeAl is lower than that of $Ni_{12}P_5$-Al_2O_3. This is because of the n-type semiconductor property of CeO_2. Indeed, when the CeO_2 is reduced, oxygen vacancies are produced, and free electrons migrate to Ni sites in nickel phosphide [38 51], leading to an increment of the electron charge density (ECD) around the $Ni_{12}P_5$. In addition, as can be seen from Table 1, the content of $Ni_{12}P_5$ in $Ni_{12}P_5$-CeAl (38%) is higher than the value in $Ni_{12}P_5$-Al_2O_3 (26%), indicating that the presence of CeO_2 in the support can help the electron transfer to Ni and stabilize $Ni_{12}P_5$ in a reduced phase from surface oxidation. In addition, it is worth noting that the intensity of Ni_2P-SiO_2 spectrum is clearly weaker than the other two catalysts. Since the intensity of XPS spectrum measures how much of a material is at the surface, the weaker intensity of Ni_2P peaks shows that the content of Ni_2P component presented on the Ni_2P-SiO_2 surface is less than the contents of $Ni_{12}P_5$ presented on the alumina containing catalysts.

3.1.3. H_2 –TPR results

H_2-TPR were conducted to gather further understanding of catalysts' redox features and the interactions among the nickel phosphide phases and the different supports. For this experiment the transformation of the catalyst precursors (before reduction) to phosphides was tracked by H_2-TPR. Fig. 4 shows hydrogen consumption profiles of the studied samples from room temperature to 920 °C. The precursor of Ni_2P-SiO_2 presents the typical reduction peak around 400 °C corresponding to the reduction of bulk NiO. The maximum peak at 700 °C corresponds to the co-reductions of the nickel species in phosphate and the P–O bond [38,52,53]. Normally, the reduction of PO_x/SiO_2 is reported to begin at about 800 °C and was not complete until 1000 °C due to the high thermally stable P-O bond [54]. However, the corresponding reduction happened at lower temperature (700 °C) in this case, indicating that the PO_x/SiO_2 phase was more easily reduced due to extra hydrogen atom availability from dissociation of H_2 on metallic Ni. Based on TPR findings, during the H_2-TPR process, Ni species were first reduced to metallic Ni, which via dissociation of H_2 appear to promote the reduction of P-O bond, in good agreement with prior findings [55].

For the precursor of $Ni_{12}P_5$-Al_2O_3, the peak centred at 690 °C was assigned to the reduction of nickel phosphate species on Al_2O_3 [38,56]. The reduction temperature of nickel species in $Ni_{12}P_5$-Al_2O_3 precursor is lower than that of Ni_2P/SiO_2 precursor because the strong interaction between Al_2O_3 and PO_4^{3-} reduced the interaction between nickel species and phosphate. Therefore, Al_2O_3 support pro- moted the reduction of nickel phosphate to a different extent [38,57]. The temperature of the main reduction peak for $Ni_{12}P_5$-CeAl precursor is even lower than that for $Ni_{12}P_5$-Al_2O_3 (670 °C) due to the enhanced redox properties ascribed to CeO_2 [58]. The surface oxygen species on CeO_2 combined with highly reactive hydrogen atoms (those from spillover) lead to the formation of OH^- species. Such OH^- species are known to facilitate the surface diffusion of hydrogen boosting the overall sample reducibility [59].

Therefore, our TPR results showcase a clear influence of the support on the reduction behaviour of the synthesised catalysts. The existence

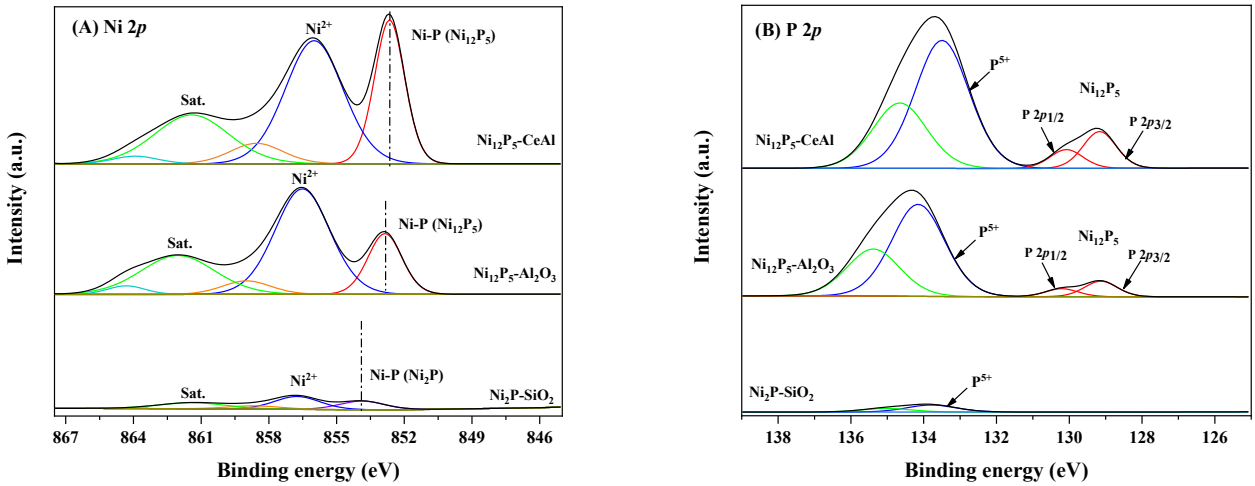

Fig. 3. X-ray photoelectron spectroscopy (XPS) Ni 2*p* spectra (A) and P 2*p* spectra (B) and the deconvoluted peaks of the Ni_2P-SiO_2, $Ni_{12}P_5$-Al_2O_3 and $Ni_{12}P_5$-CeAl.

Table 1
Binding energies and atomic proportion of relevant species of the studied samples.

Samples	Ni 2*p* 3/2 (eV)			P 2*p* (eV)		Ni/P	Ni_xP content
	Ni-P ($Ni_{12}P_5$)	Ni-P (Ni_2P)	Ni^{2+}	P^{5+}	Ni-P($Ni_{12}P_5$)		
Ni_2P-SiO_2	–	853.9 (40%)	856.8 (60%)	133.8	–	1.4	0.5%
$Ni_{12}P_5$-Al_2O_3	852.9 (26%)	–	856.5 (74%)	134.2 (91%)	129.1 (9%)	0.67	5.15%
$Ni_{12}P_5$-CeAl	852.7 (38%)	–	856 (62%)	133.5 (85%)	129.1 (15%)	0.63	11.95%

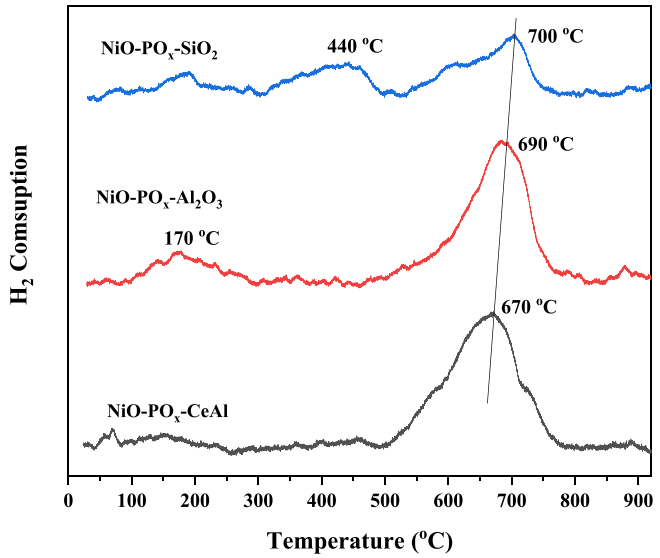

Fig.4. H_2 – Temperature-programmed reduction (TPR) results for the precursors of Ni_2P-SiO_2, $Ni_{12}P_5$-Al_2O_3 and $Ni_{12}P_5$-CeAl.

states of nickel and phosphorus species vary according to different supports after reduction.

3.1.4. *TEM results*

The nanostructure and morphology of the three fresh synthesized catalysts were investigated by TEM (as shown in Fig. 5 A, B, C) and the elements distribution of $Ni_{12}P_5$-Al_2O_3 can be seen in Fig. 5(D). Observations from TEM shows that the morphology of the nickel phosphide is greatly affected by the different supports. For $Ni_{12}P_5$-Al_2O_3 and $Ni_{12}P_5$-CeAl catalysts, large particles of $Ni_{12}P_5$ phases are observed from the outside of the support structure. According to our BET results (details presented in SI), the pore sizes of the supports are around 6–10 nm, and the nano cube size of the $Ni_{12}P_5$ structures is within the 20–50 nm range based on this TEM study, indicating that there is improvement room for the high temperature TPR synthesis process. If the precursors can be anchored inside the pores, much higher catalytic surface areas can be achieved for these catalysts. As for the Ni_2P-SiO_2 catalyst, Ni_2P attached the support as bigger chunks which have the nano size larger than 200 nm. In any case, it is very interesting to see once again that phosphides are attached but present on the surface of the supports and not in the pores. The corresponding element mappings of $Ni_{12}P_5$-Al_2O_3 shown in Fig. 5(D) confirmed that the elements of Ni and P are uniformly present on the surface of catalyst support.

3.2. *Catalytic performance*

3.2.1. *CO_2-methanation-RWGS test*

The catalytic behaviour of the prepared catalysts in terms of CO_2 conversion as a function of temperature is shown in Fig. 6 (A), whereas CO and CH_4 selectivities are shown in Fig. 6(B) and (C) respectively. All the studied catalysts are active for CO_2 upgrading via RWGS in the temperature range 300–750 °C. However, Ni_2P-SiO_2 is only active in RWGS reaction while $Ni_{12}P_5$-Al_2O_3 and $Ni_{12}P_5$-CeAl catalysts show high activities for both CO_2 methanation and RWGS reaction. The CO yield is shown in Fig. 6 (D); Ni_2P-SiO_2 exhibited higher CO yield in the 300–600 °C range.

Compared to $Ni_{12}P_5$-CeAl and $Ni_{12}P_5$-Al_2O_3, Ni_2P/SiO_2 is a more selective catalyst for RWGS, producing 80% CO in the full temperature range of 350–750 °C. This indicates a high degree of suppression of the methanation reaction by Ni_2P-SiO_2 catalyst, as Ni catalysts are known for their high methanation activity. This is shown to not simply be a site blocking effect; the nickel phosphide phase and SiO_2 support play key roles to explain the better selectivity. A similar CO selectivity towards RWGS reaction has been observed in the Ni_2P-CeO_2 catalyst synthesized by Cui *et al.* Despite Ni catalysts have been demonstrated to be highly active to CO_2 methanation, Ni_2P-CeO_2 presented high CO selectivity, better than that of the conventional Ni/CeO_2 catalyst [60]. Their results of the CO_2-TPD and H_2-TPD analysis indicated that Ni_2P/CeO_2 had a moderate CO_2 adsorption strength and a strong adsorption ability for H species. The moderately adsorbed CO_2 species were easily desorbed, on the contrary, the hydrogen species were strongly adsorbed at low reaction temperatures, preventing the CO_2 from further hydrogenating to CH_4, which lead to the remarkable CO selectivity. For the influence of SiO_2 support, Riani *et al.* explored the performance of Ni-SiO_2/Al_2O_3 catalyst for CO_2 methanation, and they found that the catalytic performance for CO_2 methanation decreased with the addition of SiO_2 to the Al_2O_3 support due to the lowered CO_2 adsorption [61]. Therefore, the combination of Ni_2P and SiO_2 support suppresses CO_2 methanation, this being an important finding for RWGS catalyst development.

$Ni_{12}P_5$-CeAl and $Ni_{12}P_5$-Al_2O_3 catalysts are also of interest as switchable catalysts due to their switchover from methanation at low temperatures to rWGS at higher temperatures. This behaviour in itself is not unique (it is predicted by thermodynamics), but the relatively low temperature light-off behaviour observed on these catalysts demonstrates good kinetics, which warrants further exploration of their use in a flexible CO and CH_4 production scenario. $Ni_{12}P_5$-CeAl exhibits higher CO_2 conversion in the whole temperature range, particularly in CO_2 methanation at 350–550 °C. The CO_2 conversion on $Ni_{12}P_5$-CeAl at 300 °C (52%) is almost double that of $Ni_{12}P_5$-Al_2O_3 (27%). This support effect is similar to what has been observed in CO_2 methanation with Ni/CeO_2 and Ni/Al_2O_3 catalysts [62]. Ni/CeO_2 showed high CO_2 conversion especially at low temperatures compared to Ni/Al_2O_3. This is because the amount of CO_2 adsorbed onto Ni/CeO_2 was much larger than that on Ni/Al_2O_3, leading to the improvement of CO_2 methanation [54]. In our case, it is considered that the coverage of CO_2 increased with the addition of CeO_2 in the support, resulting in a higher CO_2 conversion over $Ni_{12}P_5$-CeAl. In addition, the oxygen vacancies created in the ceria lattice could also enhance the catalytic activity for CO_2 methanation, being considered as preferential sites for CO_2 activation [63]. Apart from the effect of supports, it is worth noting that the concentration of $Ni_{12}P_5$ on $Ni_{12}P_5$-CeAl surface (38%) is larger than of $Ni_{12}P_5$-Al_2O_3 (26%, as can be seen in table 1). Since the $Ni_{12}P_5$ is considered as an active phase for CO_2 hydrogenation, the $Ni_{12}P_5$ concentration could be another reason why the CO_2 conversion over $Ni_{12}P_5$-CeAl is higher than over $Ni_{12}P_5$-Al_2O_3.

In terms of CO and CH_4 selectivities, both $Ni_{12}P_5$-CeAl and $Ni_{12}P_5$-Al_2O_3 catalysts display 100% CH_4 selectivity from 300 °C to 450 °C. When we move to the RWGS range 600–750 °C, both catalysts also reached highly remarkable CO selectivity. Herein, a faster selectivity switch from CH_4 to CO is achieved by the $Ni_{12}P_5$-CeAl catalyst. As can be

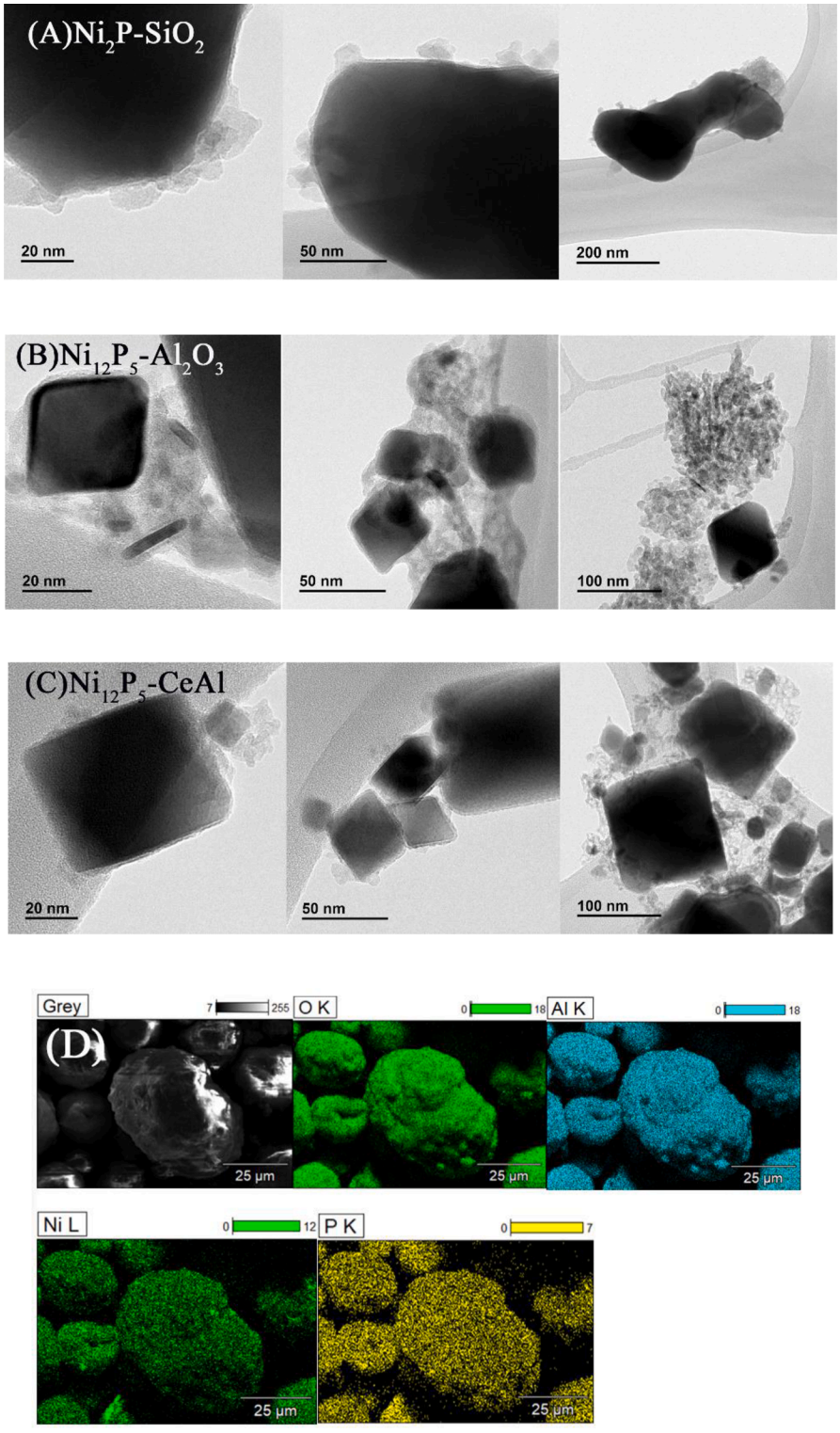

Fig. 5. TEM micrographs of (A) Ni_2P-SiO_2; (B) $Ni_{12}P_5$-Al_2O_3; (C) $Ni_{12}P_5$-CeAl (D) SEM-EDX micrographs of $Ni_{12}P_5$-Al_2O_3.

seen from Fig. 6 (B) (C): CO_2 methanation decreased from 500 °C and RWGS started to become the dominant reaction. The CO selectivity of $Ni_{12}P_5$-CeAl increased from 10% to 30% and the CH_4 selectivity decreased from 97% to 73% when the temperature changed from 500 °C to 550 °C, while the CO selectivity of $Ni_{12}P_5$-Al_2O_3 only increased by 10% and CH_4 selectivity only decreased by 5%. In addition, it is worth noting that $Ni_{12}P_5$-CeAl shows higher CO selectivity than $Ni_{12}P_5$-Al_2O_3 during the whole high temperature range (500 °C −750 °C). The better performance towards $Ni_{12}P_5$-CeAl for RWGS reaction could be attributed to the excellent redox properties of CeO_2, which enhances the Ni reducibility. CeO_2 participates the RWGS reaction as it does in the forward shift process, being one of the most promising supports for this reaction thus yielding advanced catalytic performance [64–67]. The result is also in agreement with our XPS results.

Overall, both the support and the phosphide structure appear to be intimately connected with methanation vs. RWGS activity. In order to

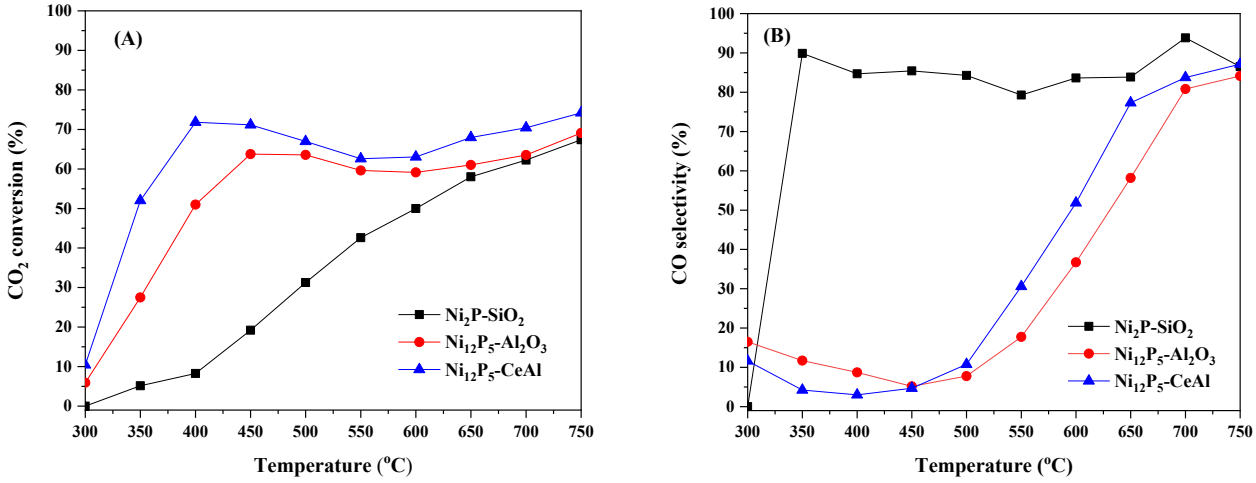

Fig. 6. (A) CO_2 conversion (B) CO selectivity (C) CH_4 selectivity and (D) CO yield for Ni_2P-SiO_2, $Ni_{12}P_5$-Al_2O_3 and $Ni_{12}P_5$-CeAl. Condition: H_2: CO_2 = 4:1, WHSV = 12000 mL $g^{-1}h^{-1}$, T: 300–750 °C.

further investigate the features of each catalyst, H_2-TPR, TPO, BET, TEM and stability tests were conducted and discussed in the following part.

3.2.2. *Stability study for switchable catalysts*

Our findings indicate that $Ni_{12}P_5$-Al_2O_3 and $Ni_{12}P_5$-CeAl demonstrate good kinetics for both methanation and RWGS. We investigated the use of the $Ni_{12}P_5$-Al_2O_3 and $Ni_{12}P_5$-CeAl for switchable operation, in a scenario where renewable hydrogen would be used to synthesise a variety of chemicals via the syngas route in addition to the direct synthesis of methane as a fuel. For such applications long-term runs are essential in catalysts' design and the stability is a major performance indicator, especially when novel formulations are developed. $Ni_{12}P_5$-CeAl and $Ni_{12}P_5$-Al_2O_3 catalysts have been subjected to long-term stability tests under methanation and RWGS conditions, simulating a switchable operation. The stability tests were conducted over four consecutive 24 h cycles. The temperature was switched from 375 °C to 700 °C to simulate the change between a methanation process and a RWGS unit under the operating conditions.

Fig. 7 (A) (B) show the conversion of CO_2 and associated products selectivity recorded during stability tests. It is clear that both catalysts exhibit very stable performance after 96 h of continuous operation in terms of CO_2 conversion and CO&CH_4 selectivities. For $Ni_{12}P_5$-Al_2O_3 (Fig. 7 (A)), the CO_2 conversion was maintained of at 68% in the RWGS zone and increased from 52% to 56% in the CO_2 methanation zone. Meanwhile, the production of CO and CH_4 were very stable. <1% stability changes were witnessed between the two CO_2 methanation and rWGS reaction cycles. For $Ni_{12}P_5$-CeAl (Fig. 7 (B)), the CO_2 conversion in the RWGS zone (67%) is nearly identical to the value of $Ni_{12}P_5$-Al_2O_3, but the CO_2 conversion in CO_2 methanation zone towards $Ni_{12}P_5$-CeAl is clearly higher than that of $Ni_{12}P_5$-Al_2O_3, which is in agreement with our temperature screening test. The CO selectivity in the RWGS zone and the CH_4 selectivity in the CO_2 methanation zone were maintained constant (98% and 86%) respectively. It is also worth noting that a slight decrease of CO_2 conversion happened in the first CO_2 methanation cycle, but after one cycle RWGS test, the CO_2 conversion increased to an even higher value in the second CO_2 methanation cycle suggesting the catalyst had stabilised. Overall, our catalysts display excellent stability under both reaction conditions, validating their switchable behaviour – a very promising result allowing end-product flexibility. Considering about the performance during whole stability process, CeAl is a better support than Al_2O_3 for $Ni_{12}P_5$ catalysts because of the higher catalytic activity exhibited in the CO_2 methanation zone.

The performances of some Ni catalysts reported recently in the literature are listed in the Table 2 below. As shown in Table 2, our catalysts show comparable performance as several nickel catalysts under the same temperature window and reaction mixture (H_2:CO_2 = 4). Our group has previously synthesized and explored the CO_2 hydrogenation activity of Ni/Al_2O_3 and Ni/CeAl [11]. The trend of CO_2 conversion and

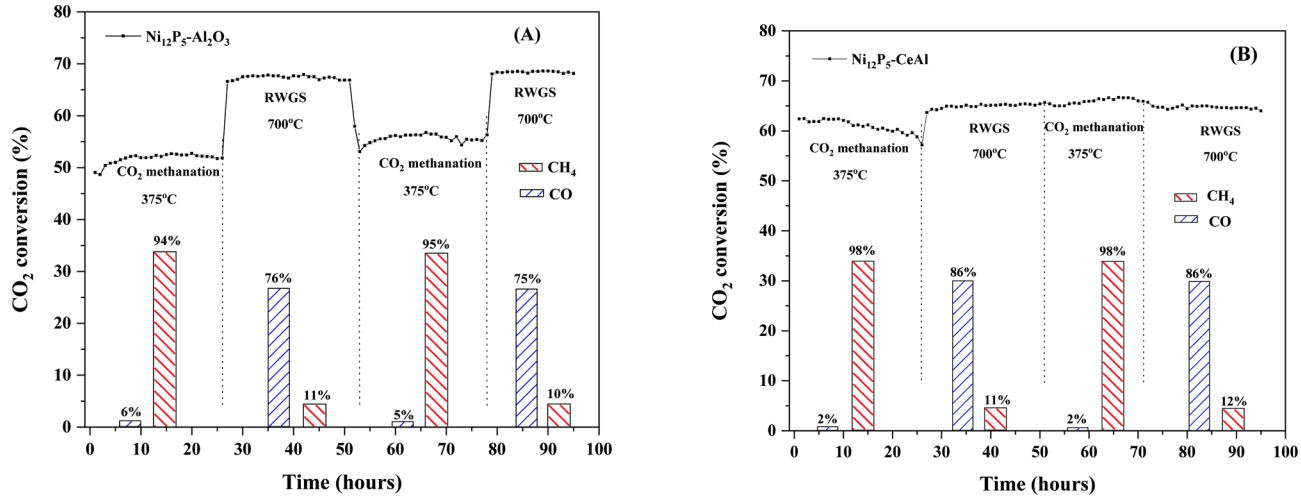

Fig. 7. Stability test at 375 °C and 700 °C, WHSV of 12,000 mL/(g·h) with a H_2: CO_2 ratio of 4:1 for (A) $Ni_{12}P_5$-Al_2O_3 (B) $Ni_{12}P_5$-CeAl.

Table 2
Catalyst performance comparison with materials reported in the literature.

Catalysts	H_2:CO_2	WHSV (mL $g^{-1}h^{-1}$)	Temperature (°C)	CO_2 conversion	CO selectivity	CH_4 selectivity	Ref
Ni_2P-SiO_2				58%	84%	6%	This work
$Ni_{12}P_5$-Al_2O_3	4	12,000	650	61%	58%	40%	
$Ni_{12}P_5$-CeAl				68%	77%	15%	
Ni/Al_2O_3	4	30,000	650	57%	64%	36%	[11]
Ni/CeAl		30,000	650	63%	75%	24%	
1%NiCo@ SiO_2	4	15,000	650	65%	82%	6%	[68]
2%NiCo@ SiO_2				65%	80%	11%	
NiCu-Saponite				68%	85%	8%	
Ni-Saponite				62%	77%	12%	
NiCo-Saponite	4	15,000	650	61%	78%	11%	[69]

CO selectivity towards Ni/CeAl and Ni/Al catalysts is in line with this work. With the addition of CeO_2 in support, both the CO_2 conversion and CO selectivity increased. However, even for the better one (Ni/CeAl), the $Ni_{12}P_5$-CeAl catalysts in this work exhibited higher CO_2 activity for both CO_2 methanation and RWGS reaction compared to the Ni/CeAl catalyst in previous work. When considering selectivity, 1%NiCo@SiO_2 reported in ref [68] display competitive selectivity (greater than80%), which is also as the same level as the CO selectivity over Ni_2P-SiO_2 in our work.

3.2.3. Stability study for Ni_2P-SiO_2

Since Ni_2P-SiO_2 is an excellent catalyst for RWGS leading to the total suppression of side reactions, a 48 h stability test was also conducted for Ni_2P-SiO_2 with a H_2: CO_2 ratio of 4:1 at WHSV of 12,000 mL $g^{-1}h^{-1}$. As the results show in Fig. 8 (A) (B), the CO_2 conversion dramatically declined from 48% to 32% in the first 5 h. After 5 h, the trend gradually flattened, but the decrease still continued. At the end of the 48 h test, the CO_2 conversion halved from 48% to 23%. Meanwhile, CO selectivity increased and CH_4 selectivity decreased during the process.

3.3. Post-reaction characterisation of catalysts

3.3.1. TPO results

TPO experiments of the catalysts after stability tests were performed and the evolution of CO_2 signal ($m/z = 44$) was analysed by MS, and the results are shown in Fig. 9. According to previous studies, certain temperature ranges of CO_2 peaks can be assigned to the different type of carbonaceous species. The peaks appeared lower than 380 °C are attributed to monoatomic and polymeric carbon [70,71], which are the active intermediates in the CO_2-methanation-RWGS reaction. The second range peaks between 440 °C and 640 °C are assigned to whisker carbon formed on or close to Ni particles [72]. In general, the most stable carbon is the graphitic carbon formed on the support (temperature range: TPO greater than 650 °C), which does not appear in these

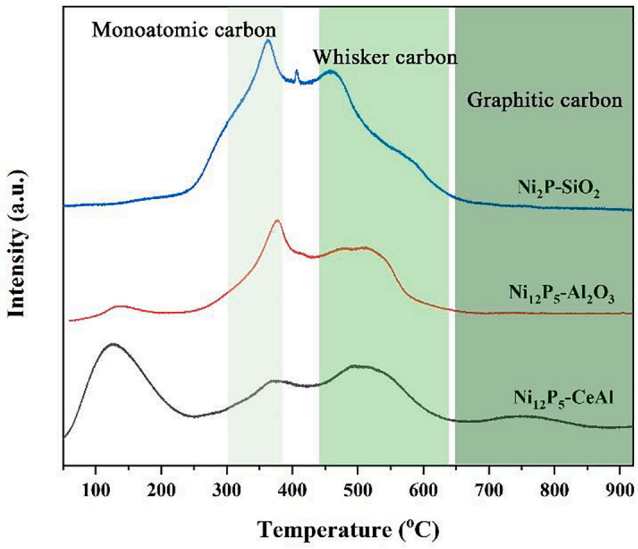

Fig. 9. Temperature-programmed oxidation (TPO) results for post-stability Ni_2P-SiO_2, $Ni_{12}P_5$-Al_2O_3 and $Ni_{12}P_5$-CeAl.

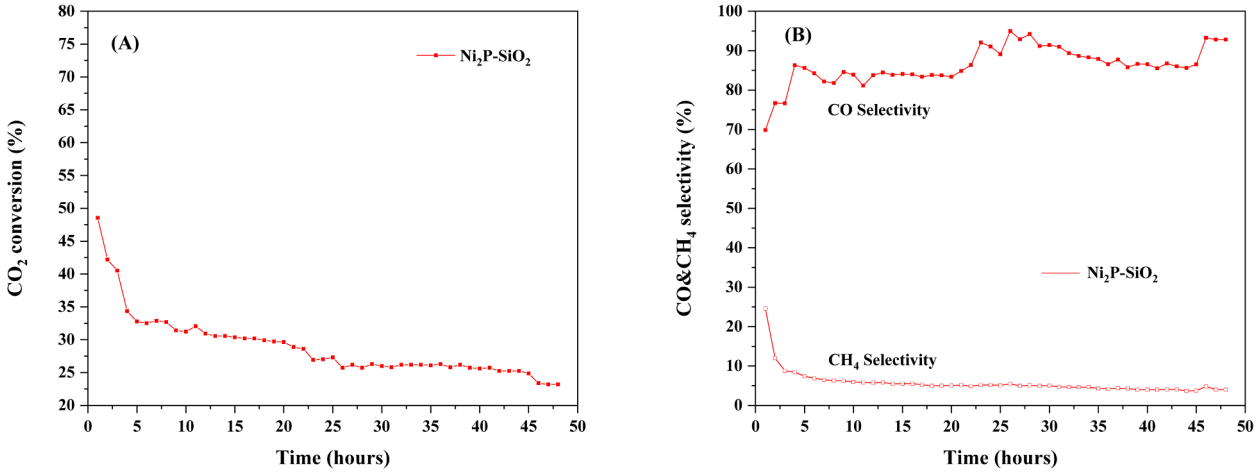

Fig.8. Stability test at 550 °C, WHSV of 12,000 mL/(g·h) with a H_2: CO_2 ratio of 4:1 for Ni_2P-SiO_2 (A) CO_2 conversion for Ni_2P/SiO_2 (B) CO&CH_4 selectivity for Ni_2P/SiO_2.

three catalysts [73,74]. Since the carbon formed on and near the metal could be burned at lower temperature than the carbon formed on the support, the carbonaceous species in this case can be removed from the catalysts surface at a comparatively low temperature (below 600 °C).

3.3.2. TGA results

In order to further quantify the carbon deposition, TGA tests were carried out and the results are shown in Fig. 10. All the samples used in this section are post stability samples. Ni_2P-SiO_2 system was tested for 48 h at 550 °C, WHSV of 12,000 mL/(g·h) with a H_2: CO_2 ratio of 4:1 while $Ni_{12}P_5$-Al_2O_3 and $Ni_{12}P_5$-CeAl samples were tested for 96 h at 375 °C and 700 °C (48 h for each temperature) under same inlet gas condition.

As shown in Fig. 11, most of the carbon combustion happens in the temp range 0–300 °C. For the Ni_2P-SiO_2 catalyst, we observe that the weight loss caused by coking is 5% (Fig. 10A). The same value for $Ni_{12}P_5$-Al_2O_3 and $N_{12}P_5$-CeAl samples are around 7% and 5.5% (Fig. 10B, 10C). Since the Ni_2P-SiO_2 sample has only been tested for 48 h, half of the stability time of $Ni_{12}P_5$-Al_2O_3 and $N_{12}P_5$-CeAl samples, we conclude that $Ni_{12}P_5$-CeAl exhibits the best performance in terms of the carbon deposition resistance. When the temperature reached at 700 °C, there are small mass increases for all these three samples, which could be assigned to the oxidation of nickel phosphide phase.

Overall, the carbon deposition happening on the surface of the synthesized catalysts is limited and the deposited carbon could be easily removed (<300 °C) indicating the suitability of these catalysts for long-term operations.

3.3.3. XRD patterns for post reaction and stability test samples

To investigate the phase changes happened during the CO_2-methanation-RWGS reaction and stability tests, the XRD patterns of the catalysts after CO_2-methanation-RWGS reaction and stability tests are shown in Fig. 11 (A) and (B) respectively. Apart from the SiO_2, Al_2O_3 and $Ni_{12}P_5$ compounds observed prior to reaction (Fig. 2), all diffraction peaks labelled by yellow dots in $Ni_{12}P_5$-Al_2O_3 and $Ni_{12}P_5$-CeAl samples should be attributed to Ni_3P (JCPDS No. 34–0501) [75,76].

For the post reaction samples, very interestingly, despite the initial differences in their initial structure, catalytic testing induces a phase change in all studied catalysts. Ni_2P evolves into $Ni_{12}P_5$ in Ni_2P-SiO_2 catalyst while most diffraction peaks of $Ni_{12}P_5$ phase disappear and Ni_3P became the main phase in spent $Ni_{12}P_5$-Al_2O_3 and $Ni_{12}P_5$-CeAl samples. The phase changes could be due to the increased temperature during the catalytic test (up to 750 °C in RWGS), which is higher than the reduction temperature in the synthesis (650 °C). According to the TPR results, the reduction of nickel phosphate continued to 750 °C, hence, these catalysts have been reduced further with the constant H_2 input and the elevated temperature of 750 °C. Also, it is worth noting that metal-rich phase appeared after CO_2-methanation-RWGS reaction. According to the previous research [77], during the temperature-programmed reduction of nickel phosphate, PH_3 and P^{n+} species appeared in the gas flows from very low temperatures (200 °C) and increased significantly above 510 °C. PH_3 is formed by the reduction of phosphate precursors in H_2, and the reaction of PH_3 with H_2O yields P^{n+} species. PH_3 was involved in the formation of phosphide phases. Hence, the disproportionation of the phosphide can be attributed to the generation of PH_3 and P^{n+} species from the continuous H_2 reduction in RWGS. However, stabilised performance was observed during extended testing so it is worth noting that the loss of P may not be continuous.

Compared with the XRD pattern of post reaction Ni_2P-SiO_2, there is no big difference observed in the XRD of post stability sample. However, the CO_2 conversion over Ni_2P-SiO_2 decreased rapidly in the initial hours of the stability test. For the post-stability $Ni_{12}P_5$-Al_2O_3 and $Ni_{12}P_5$-CeAl samples, more $Ni_{12}P_5$ peaks disappeared compared to XRD patterns of the post reaction samples, indicating further reduction from $Ni_{12}P_5$ phase to Ni_3P happened during the long-term run. Such further reduction increases Ni electronic density favouring CO_2 activation by electron donation to the π* antibonding orbitals of CO_2 weaking the C-O bond and favouring both methanation and RWGS reactions. Indeed, for similar reasons, Ni_3P has been shown to be highly active in the hydrodeoxygenation reaction where an electronically rich Ni catalyses the C-O and O–H bonds cleavage [78]. In addition, compared to the XRD of fresh $Ni_{12}P_5$-CeAl (Fig. 2), crystalline CeO_2 disappeared after the stability test, indicating that sintering happened during the stability test.

Based on the XRD test of the post reaction and stability samples, it is worth pointing out that these catalysts are interesting candidates for operando spectroscopic investigations to better understand the key active phases associated with RWGS and methanation activity and for improved rational design by stabilising these active sites. Our group has explored the mechanism of RWGS towards Ni_2P catalysts by using density functional theory (DFT) research previously. The results show that Ni_2P favours the COOH-mediated path and the reaction step for the formation of COOH* intermediate may be considered as the main rate-determining step on Ni_2P (0001) in RWGS reaction. As for the formation of CH_4, CO hydrogenates to form the CHO* intermediate, then dissociates to form CH* and O* species on the surface. Here the CH* species gets sequentially hydrogenated which leads to formation of CH_4 on the Ni_2P (0001) surface [79]. In addition, it is widely accepted that the further hydrogenation and dissociation ability of CO rather than CO_2 on the catalyst affects the formation of the final product [80,81]. The mechanism of CO&CH_4 formation towards $Ni_{12}P_5$ surface will be included in our ongoing projects. In addition, in order to achieve better control over phosphide phase and particle size irrespective of support, colloidal synthesis techniques can be used in the future work, where the phosphide nanoparticles are first synthesised in solution and then impregnated onto different supports [82]. This method has been used to successfully synthesize MoP catalysts for CO_2 hydrogenation [83].

4. Conclusions

This work showcases a strategy to design highly effective CO_2 conversion catalysts for combined CO_2-methanation-RWGS schemes. Such strategy relies on the presence of an adequate switchable catalyst able to efficiently catalyse both reactions. Herein, we report innovative Ni phosphide-based systems with high CO_2 conversion activity and remarkable selectivity towards the desired end products (CH_4 and CO). We observe a strong influence of the support, which plays a role in both

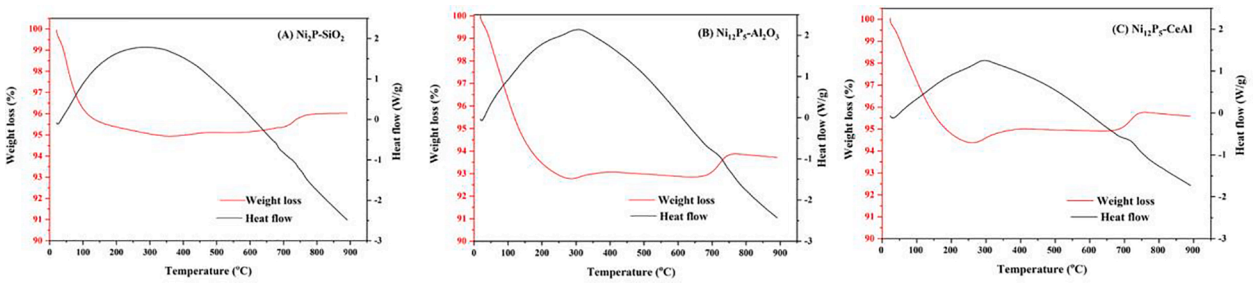

Fig. 10. Thermogravimetric analysis (TGA) and differential scanning calorimetry (DSC) for post stability (A) Ni_2P-SiO_2, (B) $Ni_{12}P_5$-Al_2O_3 and (C) $Ni_{12}P_5$-CeAl.

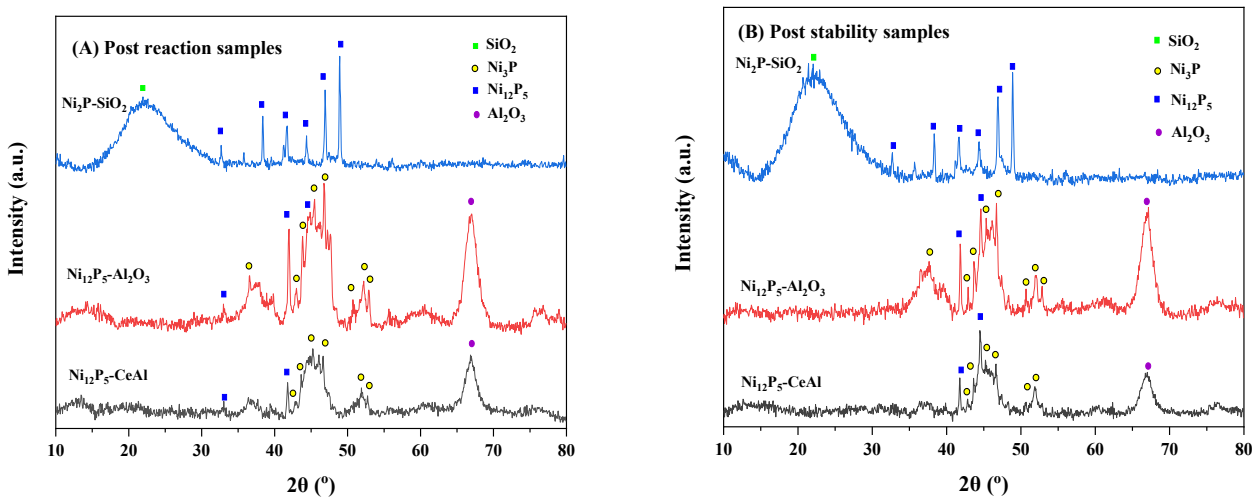

Fig. 11. X-ray diffraction patterns for (A) Post reaction samples, and (B) Post stability test samples.

the phosphide phase formed during synthesis as well as the catalytic activity for methanation and rWGS. We report the remarkable total selectivity of Ni_2P/SiO_2 to CO even at the low temperatures that favour methanation, which demonstrates a significant shift from other Ni-based catalysts. Phosphide formation emerges as a significant means to fine tune catalytic activity, with the extent of phosphidation and support-phosphide interaction determining performance. $Ni_{12}P_5$ and Ni_3P structures found in the alumina-containing samples (either bare alumina or ceria-alumina mixtures) yield a switchable behaviour with good CO_2 conversion levels and high selectivity to CO/CH_4 that can be controlled by adjusting temperature. The support and the active phase present in the sample also affects the carbon deposition and potential catalysts deactivation-regeneration.

Among the studied samples $Ni_{12}P_5$-CeAl is the best performing catalyst for flexible chemical synthesis displaying excellent activity, selectivity and long-term stability. However, we report for the first time the excellent RWGS activity for Ni_2P/SiO_2, which can have applications for large scale CO synthesis and tandem catalysis schemes where selective CO synthesis at low temperatures will be essential. Ni-phosphides are underexplored for these applications and we aim to spark interests within the catalysis community towards these very promising materials to develop disruptive approaches for CO_2 valorisation in the context of a circular economy.

Declaration of Competing Interest

The authors declare that they have no known competing financial interests or personal relationships that could have appeared to influence the work reported in this paper.

Acknowledgements

Financial support for this work was provided by the Department of Chemical and Process Engineering at the University of Surrey and CO2ChemUK through the EPSRC grant EP/P026435/1 as well as the Royal Society Research Grant RSGR1180353. This work was also partially sponsored by Ministry of Science and Innovation through the projects PID2019-108453 GB-C21 and JC2019-040560-I. This work was also partially sponsored by the European Commission through the H2020-MSCA-RISE-2020 BIOALL project (Grant Agreement: 101008058. SASOL is also acknowledged for kindly providing the Al_2O_3-based supports.

Appendix A. Supplementary data

Supplementary data to this article can be found online at https://doi.org/10.1016/j.fuel.2022.124301.

References:

[1] Wei W, Jinlong G. Methanation of carbon dioxide: an overview. Front Chem Sci Eng 2011;5(1):2–10. https://doi.org/10.1007/s11705-010-0528-3.
[2] Huang CH, Tan CS. A review: CO_2 utilization. Aerosol Air Qual Res 2014;14(2):480–99. https://doi.org/10.4209/aaqr.2013.10.0326.
[3] Bose BK. Global Warming: Energy, Environmental Pollution, and the Impact of Power Electronics. IEEE Ind Electron Mag 2010;4(1):6–17. https://doi.org/10.1109/MIE.2010.935860.
[4] Solomon CG, Haines A, Ebi K. The Imperative for Climate Action to Protect Health. N Engl J Med 2019;380(3):263–73. https://doi.org/10.1056/NEJMra1807873.
[5] Daza YA, Kent RA, Yung MM, Kuhn JN. Carbon dioxide conversion by reverse water-gas shift chemical looping on perovskite-type oxides. Ind Eng Chem Res 2014;53(14):5828–37. https://doi.org/10.1021/ie5002185.
[6] Thema M, Bauer F, Sterner M. Power-to-Gas: Electrolysis and methanation status review. Renew Sustain Energy Rev 2019;112(May):775–87. https://doi.org/10.1016/j.rser.2019.06.030.
[7] le Saché E, Pastor-Pérez L, Haycock BJ, Villora-Picó JJ, Sepúlveda-Escribano A, Reina TR. Switchable Catalysts for Chemical CO_2 Recycling: A Step Forward in the Methanation and Reverse Water-Gas Shift Reactions. ACS Sustainable Chem Eng 2020;8(11):4614–22. https://doi.org/10.1021/acssuschemeng.0c00551110.1021/acssuschemeng.0c00551.s001.
[8] Su X, Xu J, Liang B, Duan H, Hou B, Huang Y. Catalytic carbon dioxide hydrogenation to methane: A review of recent studies. Journal of Energy Chemistry 2016;25(4):553–65. https://doi.org/10.1016/j.jechem.2016.03.009.
[9] Schiebahn S, Grube T, Robinius M, Tietze V, Kumar B, Stolten D. Power to gas: Technological overview, systems analysis and economic assessment for a case study in Germany. Int J Hydrogen Energy 2015;40(12):4285–94. https://doi.org/10.1016/j.ijhydene.2015.01.123.
[10] Sun F-M, Yan C-F, Wang Z-d, Guo C-Q, Huang S-L. Ni/Ce–Zr–O catalyst for high CO_2 conversion during reverse water gas shift reaction (RWGS). Int J Hydrogen Energy 2015;40(46):15985–93. https://doi.org/10.1016/j.ijhydene.2015.10.004.
[11] Yang L, Pastor-Pérez L, Gu S, Sepúlveda-Escribano A, Reina TR. Highly efficient Ni/CeO_2-Al_2O_3.catalysts for CO_2 upgrading via reverse water-gas shift: Effect of selected transition metal promoters. Appl Catal B 2018;232(January):464–71. https://doi.org/10.1016/j.apcatb.2018.03.091.
[12] Martínez J, Hernández E, Alfaro S, López Medina R, Valverde Aguilar G, Albiter E, et al. High Selectivity and Stability of Nickel Catalysts for CO_2 Methanation: Support Effects. Catalysts 2019;9(1):24. https://doi.org/10.3390/catal9010024.
[13] Guharoy U, Ramirez Reina T, Olsson E, Gu S, Cai Q. Theoretical Insights of Ni_2P (0001) Surface toward Its Potential Applicability in CO_2 Conversion via Dry Reforming of Methane. ACS Catal 2019;9(4):3487–97. https://doi.org/10.1021/acscatal.8b0442310.1021/acscatal.8b04423.s001.
[14] González-Castaño M, Saché EL, Berry C, Pastor-pérez L, Arellano-garcía H, Wang Q, et al. Nickel phosphide catalysts as efficient systems for CO_2 upgrading via dry reforming of methane. Catalysts 2021;11(4):1–11. https://doi.org/10.3390/catal11040446.
[15] Zhao HY, Li D, Bui P, Oyama ST. Hydrodeoxygenation of guaiacol as model compound for pyrolysis oil on transition metal phosphide hydroprocessing catalysts. Appl Catal A 2011;391(1–2):305–10. https://doi.org/10.1016/j.apcata.2010.07.039.

[16] Yu Z, Wang Y, Sun Z, Li X, Wang A, Camaioni DM, et al. Ni_3P as a high-performance catalytic phase for the hydrodeoxygenation of phenolic compounds. Green Chem 2018;20(3):609–19. https://doi.org/10.1039/C7GC03262E.

[17] Wu HC, Chang YC, Wu JH, Lin JH, Lin IK, Chen CS. Methanation of CO_2 and reverse water gas shift reactions on Ni/SiO_2 catalysts: the influence of particle size on selectivity and reaction pathway. Catal Sci Technol 2015;5(8):4154–63. https://doi.org/10.1039/C5CY00667H.

[18] Pastor-Pérez L, Shah M, Le Saché E, Ramirez Reina T. Improving Fe/Al_2O_3 catalysts for the reverse water-gas shift reaction: on the effect of Cs as activity/selectivity promoter. Catalysts 2018;8(12):608. https://doi.org/10.3390/catal8120608.

[19] Pastor-Pérez L, Baibars F, Le Sache E, Arellano-García H, Gu S, Reina TR. CO_2 valorisation via reverse water-gas shift reaction using advanced Cs doped Fe-Cu/Al_2O_3 catalysts. Journal of CO_2 utilization 2017;21:423–8. https://doi.org/10.1016/j.jcou.2017.08.009.

[20] Dai B, Zhou G, Ge S, Xie H, Jiao Z, Zhang G, et al. CO_2 reverse water-gas shift reaction on mesoporous M-CeO_2 catalysts. The Canadian Journal of Chemical Engineering 2017;95(4):634–42. https://doi.org/10.1002/cjce.v95.410.1002/cjce:22730.

[21] Yang L, Pastor-Pérez L, Villora-Pico JJ, Gu S, Sepúlveda-Escribano A, Reina TR. CO_2 valorisation via reverse water-gas shift reaction using promoted Fe/CeO_2-Al_2O_3 catalysts: Showcasing the potential of advanced catalysts to explore new processes design. Appl Catal A 2020;593:117442. https://doi.org/10.1016/j.apcata.2020.117442.

[22] Wang J-Y, Zeng C-Y, Wu C-Z. Silica-modified Cu–ZnO/HZSM–5 catalyst and its catalytic performance in dimethyl ether synthesis from CO_2 hydrogenation. J Fuel Chem Technol 2006;34:195–9.

[23] Garbarino G, Wang C, Cavattoni T, Finocchio E, Riani P, Flytzani-Stephanopoulos M, et al. A study of Ni/La-Al_2O_3 catalysts: a competitive system for CO_2 methanation. Appl Catal B 2019;248:286–97. https://doi.org/10.1016/j.apcatb.2018.12.063.

[24] Yang L, Pastor-Pérez L, Gu S, Sepúlveda-Escribano A, Reina TR. Highly efficient Ni/CeO_2-Al_2O_3 catalysts for CO_2 upgrading via reverse water-gas shift: Effect of selected transition metal promoters. Appl Catal B 2018;232(January):464–71. https://doi.org/10.1016/j.apcatb.2018.03.091.

[25] Oyama ST, Wang X, Lee YK, Bando K, Requejo FG. Effect of phosphorus content in nickel phosphide catalysts studied by XAFS and other techniques. J Catal 2002;210(1):207–17. https://doi.org/10.1006/jcat.2002.3681.

[26] Huang J, Li F, Liu B, Zhang P. Ni_2P/rGO/NF nanosheets as a bifunctional high-performance electrocatalyst for water splitting. Materials 2020;13(3):1–10. https://doi.org/10.3390/ma13030744.

[27] Lan, X., Hensen, E. J. M., & Weber, T. (2018). Hydrodeoxygenation of guaiacol over Ni_2P/SiO_2–reaction mechanism and catalyst deactivation. Applied Catalysis A: General, 550(October 2017), 57–66. https://doi.org/10.1016/j.apcata.2017.10.018.

[28] Wu ZG, Jia YR, Wang J, Guo Y, Gao JF. Core-shell SiO_2/Ag composite spheres: Synthesis, characterization and photocatalytic properties. Materials Science-Poland 2016;34(4):806–10. https://doi.org/10.1515/msp-2016-0121.

[29] Iino A, Cho A, Takagaki A, Kikuchi R, Oyama ST. Kinetic studies of hydrodeoxygenation of 2-methyltetrahydrofuran on a Ni_2P/SiO_2 catalyst at medium pressure. J Catal 2014;311:17–27. https://doi.org/10.1016/j.jcat.2013.11.002.

[30] Liu D, Wang A, Liu C, Prins R. Ni_2P/Al_2O_3 hydrodesulfurization catalysts prepared by separating the nickel compound and hypophosphite. Catal Today 2017;292:133–42. https://doi.org/10.1016/j.cattod.2016.09.019.

[31] Deliy I, Shamanaev I, Aleksandrov P, Gerasimov E, Pakharukova V, Kodenev E, et al. Support effect on the performance of Ni_2P catalysts in the hydrodeoxygenation of methyl palmitate. Catalysts 2018;8(11):515. https://doi.org/10.3390/catal8110515.

[32] Pan Y, Liu Y, Zhao J, Yang K, Liang J, Liu D, et al. Monodispersed nickel phosphide nanocrystals with different phases: Synthesis, characterization and electrocatalytic properties for hydrogen evolution. J Mater Chem A 2015;3(4):1656–65. https://doi.org/10.1039/C4TA04867A.

[33] Ma R, Islam MJ, Reddy DA, Kim TK. Transformation of CeO_2 into a mixed phase CeO_2/Ce_2O_3 nanohybrid by liquid phase pulsed laser ablation for enhanced photocatalytic activity through Z-scheme pattern. Ceram Int 2016;42(16):18495–502. https://doi.org/10.1016/j.ceramint.2016.08.186.

[34] Yang Z-M, Huang G-F, Huang W-Q, Wei J-M, Yan X-G, Liu Y-Y, et al. Novel Ag_3PO_4/CeO_2 composite with high efficiency and stability for photocatalytic applications. J Mater Chem A 2014;2(6):1750–6. https://doi.org/10.1039/C3TA14286H.

[35] Mi K, Ni Y, Hong J. Solvent-controlled syntheses of $Ni_{12}P_5$ and Ni_2P nanocrystals and photocatalytic property comparison. J Phys Chem Solids 2011;72(12):1452–6. https://doi.org/10.1016/j.jpcs.2011.08.028.

[36] Liu P, Zhang ZX, Jun SW, Zhu YL, Li YX. Controlled synthesis of nickel phosphide nanoparticles with pure-phase Ni_2P and $Ni_{12}P_5$ for hydrogenation of nitrobenzene. Reaction Kinetics, Mechanisms and Catalysis 2019;126(1):453–61. https://doi.org/10.1007/s11144-018-1496-8.

[37] Alvarez-Galvan M, Campos-Martin J, Fierro J. Transition metal phosphides for the catalytic hydrodeoxygenation of waste oils into green diesel. Catalysts 2019;9(3):293. https://doi.org/10.3390/catal9030293.

[38] Shi H, Chen J, Yang Y, Tian S. Catalytic deoxygenation of methyl laurate as a model compound to hydrocarbons on nickel phosphide catalysts: Remarkable support effect. Fuel Process Technol 2014;118:161–70. https://doi.org/10.1016/j.fuproc.2013.08.010.

[39] Chen J, Shi H, Li L, Li K. Deoxygenation of methyl laurate as a model compound to hydrocarbons on transition metal phosphide catalysts. Appl Catal B 2014;144:870–84. https://doi.org/10.1016/j.apcatb.2013.08.026.

[40] Cecilia JA, Infantes-Molina A, Rodríguez-Castellón E, Jiménez-López A, Oyama ST. Oxygen-removal of dibenzofuran as a model compound in biomass derived bio-oil on nickel phosphide catalysts: Role of phosphorus. Appl Catal B 2013;136–137:140–9. https://doi.org/10.1016/j.apcatb.2013.01.047.

[41] Zhang Z, Tang M, Chen J. Effects of P/Ni ratio and Ni content on performance of γ-Al_2O_3-supported nickel phosphides for deoxygenation of methyl laurate to hydrocarbons. Appl Surf Sci 2016;360:353–64. https://doi.org/10.1016/j.apsusc.2015.10.182.

[42] Ten Have IC, Valle E, Gallo A, Snider JL, Duyar MS, Jaramillo TF. Development of Molybdenum Phosphide Catalysts for Higher Alcohol Synthesis from Syngas by Exploiting Support and Promoter Effects. Energy Technology 2019;7(5):1–14. https://doi.org/10.1002/ente.201801102.

[43] Huang Z, Chen Z, Chen Z, Lv C, Meng H, Zhang C. Ni12P5 nanoparticles as an efficient catalyst for hydrogen generation via electrolysis and photoelectrolysis. ACS Nano 2014;8(8):8121–9. https://doi.org/10.1021/nn5022204.

[44] Zhou W, Xin H, Yang H, Du X, Yang R, Li D, et al. The deoxygenation pathways of palmitic acid into hydrocarbons on silica-supported $Ni_{12}P_5$ and Ni_2P catalysts. Catalysts 2018;8(4):15–8. https://doi.org/10.3390/catal8040153.

[45] Sawhill SJ, Layman KA, Van Wyk DR, Engelhard MH, Wang C, Bussell ME. Thiophene hydrodesulfurization over nickel phosphide catalysts: Effect of the precursor composition and support. J Catal 2005;231(2):300–13. https://doi.org/10.1016/j.jcat.2005.01.020.

[46] Landau MV, Herskowitz M, Hoffman T, Fuks D, Liverts E, Vingurt D, et al. Ultradeep hydrodesulfurization and adsorptive desulfurization of diesel fuel on metal-rich nickel phosphides. Ind Eng Chem Res 2009;48(11):5239–49. https://doi.org/10.1021/ie9000579.

[47] Xie S, Gou J. Facile synthesis of $Ni_2P/Ni_{12}P_5$ composite as long-life electrode material for hybrid supercapacitor. J Alloy Compd 2017;713:10–7. https://doi.org/10.1016/j.jallcom.2017.04.170.

[48] Xu X, Du P, Guo T, Zhao B, Wang H, Huang M. In situ Grown Ni phosphate@$Ni_{12}P_5$ Nanorod Arrays as a Unique Core-Shell Architecture: Competitive Bifunctional Electrocatalysts for Urea Electrolysis at Large Current Densities. ACS Sustainable Chem Eng 2020;8(19):7463–71. https://doi.org/10.1021/acssuschemeng.0c0181410.1021/acssuschemeng.0c01814.s001.

[49] Wang Z, Wang S, Ma L, Guo Y, Sun J, Zhang N, et al. Water-Induced Formation of Ni_2P–$Ni_{12}P_5$ Interfaces with Superior Electrocatalytic Activity toward Hydrogen Evolution Reaction. Small 2021;17(6):2006770. https://doi.org/10.1002/smll.v17.610.1002/smll.202006770.

[50] Liu P, Rodriguez JA, Takahashi Y, Nakamura K. Water–gas-shift reaction on a Ni_2P (001) catalyst: Formation of oxy-phosphides and highly active reaction sites. J Catal 2009;262(2):294–303. https://doi.org/10.1016/j.jcat.2009.01.006.

[51] Li X, Zhang Y, Wang A, Wang Y, Hu Y. Influence of TiO_2 and CeO_2 on the hydrogenation activity of bulk Ni_2P. Catal Commun 2010;11(14):1129–32. https://doi.org/10.1016/j.catcom.2010.06.006.

[52] Li K, Wang R, Chen J. Hydrodeoxygenation of anisole over silica-supported Ni_2P, MoP, and NiMoP catalysts. Energy Fuels 2011;25(3):854–63. https://doi.org/10.1021/ef101258j.

[53] Pan Z, Wang R, Nie Z, Chen J. Effect of a second metal (Co, Fe, Mo and W) on performance of Ni_2P/SiO_2 for hydrodeoxygenation of methyl laurate. Journal of Energy Chemistry 2016;25(3):418–26. https://doi.org/10.1016/j.jechem.2016.02.007.

[54] Clause O, Bonneviot L, Che M. Effect of the preparation method on the thermal stability of silica-supported nickel oxide as studied by EXAFS and TPR techniques. J Catal 1992;138(1):195–205. https://doi.org/10.1016/0021-9517(92)90017-C.

[55] Oyama ST, Wang X, Lee YK, Bando K, Requejo FG. Effect of phosphorus content in nickel phosphide catalysts studied by XAFS and other techniques. J Catal 2002;210:207–17. https://doi.org/10.1006/jcat.2002.3681.

[56] Chen J, Zhou S, Ci D, Zhang J, Wang R, Zhang J. Influence of supports on structure and performance of nickel phosphide catalysts for hydrodechlorination of chlorobenzene. Ind Eng Chem Res 2009;48(8):3812–9. https://doi.org/10.1021/ie8018643.

[57] Bui P, Cecilia JA, Oyama ST, Takagaki A, Infantes-Molina A, Zhao H, et al. Studies of the synthesis of transition metal phosphides and their activity in the hydrodeoxygenation of a biofuel model compound. J Catal 2012;294:184–98. https://doi.org/10.1016/j.jcat.2012.07.021.

[58] Chen J, Wu Q, Zhang J, Zhang J. Effect of preparation methods on structure and performance of Ni/$Ce_{0.75}Zr_{0.25}O_2$ catalysts for CH_4-CO_2 reforming. Fuel 2008;87(13–14):2901–7. https://doi.org/10.1016/j.fuel.2008.04.015.

[59] Martin D, Duprez D. Mobility of surface species on oxides. 2. Isotopic exchange of D2 with H of SiO_2, Al_2O_3, ZrO_2, MgO, and CeO_2: Activation by rhodium and effect of chlorine. J Phys Chem B 1997;101(22):4428–36. https://doi.org/10.1021/jp970050z.

[60] Cui S, Wang X, Wang L, Zheng X. Enhanced selectivity of the CO_2 reverse water-gas reaction over a Ni_2P/CeO_2 catalyst. Dalton Trans 2021;50(17):5978–87. https://doi.org/10.1039/D1DT00424G.

[61] Riani, P., Valsamakis, I., Cavattoni, T., Sanchez Escribano, V., Busca, G., & Garbarino, G. (2021). Ni/SiO2-Al2O3 catalysts for CO2 methanation: Effect of La_2O_3 addition. Applied Catalysis B: Environmental, 284(August 2020). https://doi.org/10.1016/j.apcatb.2020.119697.

[62] Tada S, Shimizu T, Kameyama H, Haneda T, Kikuchi R. Ni/CeO_2 catalysts with high CO_2 methanation activity and high CH_4 selectivity at low temperatures. Int J Hydrogen Energy 2012;37(7):5527–31. https://doi.org/10.1016/j.ijhydene.2011.12.122.

[63] Trovarelli A, de Leitenburg C, Dolcetti G, Lorca JL. CO_2 methanation under transient and steady-state conditions over Rh/CeO_2 and CeO_2-Promoted Rh/SiO_2: The role of surface and bulk ceria. In Journal of Catalysis (Vol 1995;151(1): 111–24. https://doi.org/10.1006/jcat.1995.1014.

[64] Lee SM, Eom H, Kim SS. A study on the effect of CeO_2 addition to a Pt/TiO_2 catalyst on the reverse water gas shift reaction. Environmental Technology (United Kingdom) 2021;42(2):182–92. https://doi.org/10.1080/09593330.2019.1625954.

[65] Tabakova T, Manzoli M, Paneva D, Boccuzzi F, Idakiev V, Mitov I. CO-free hydrogen production over Au/CeO_2-Fe_2O_3 catalysts: Part 2. Impact of the support composition on the performance in the water-gas shift reaction. Appl Catal B 2011; 101(3–4):266–74. https://doi.org/10.1016/j.apcatb.2010.10.016.

[66] Reina TR, Ivanova S, Centeno MA, Odriozola JA. The role of Au, Cu & CeO_2 and their interactions for an enhanced WGS performance. Appl Catal B 2016;187: 98–107. https://doi.org/10.1016/j.apcatb.2016.01.031.

[67] Reina TR, Ivanova S, Laguna OH, Centeno MA, Odriozola JA. WGS and CO-PrO_x reactions using gold promoted copper-ceria catalysts: "Bulk CuO-CeO_2 vs. CuO-CeO_2/Al_2O_3 with low mixed oxide content". Appl Catal B 2016;197:62–72. https://doi.org/10.1016/j.apcatb.2016.03.022.

[68] Price, C. A. H., Pastor-Perez, L., Reina, T. R., & Liu, J. (2022). Yolk-Shell structured NiCo@SiO2 nanoreactor for CO2 upgrading via reverse water-gas shift reaction. Catalysis Today, 383(April 2020), 358–367. https://doi.org/10.1016/j.cattod.2020.09.018.

[69] Nityashree, N., Price, C. A. H., Pastor-Perez, L., Manohara, G. V., Garcia, S., Maroto-Valer, M. M., & Reina, T. R. (2020). Carbon stabilised saponite supported transition metal-alloy catalysts for chemical CO2 utilisation via reverse water-gas shift reaction. Applied Catalysis B: Environmental, 261(July 2019), 118241. https://doi.org/10.1016/j.apcatb.2019.118241.

[70] Großmann K, Dellermann T, Dillig M, Karl J. Coking behavior of nickel and a rhodium based catalyst used in steam reforming for power-to-gas applications. Int J Hydrogen Energy 2017;42(16):11150–8. https://doi.org/10.1016/j.ijhydene.2017.02.073.

[71] Schulz LA, Kahle LCS, Delgado KH, Schunk SA, Jentys A, Deutschmann O, et al. On the coke deposition in dry reforming of methane at elevated pressures. Appl Catal A 2015;504:599–607. https://doi.org/10.1016/j.apcata.2015.03.002.

[72] Therdthianwong S, Summaprasit N. Synthesis Gas Production from CH_4 Reforming with CO_2 over Pd/Al_2O_3 Promoted with CeO_2. Asian J Energy Environ 2002;3 (1–2):1–25.

[73] Parizotto NV, Rocha KO, Damyanova S, Passos FB, Zanchet D, Marques CMP, et al. Alumina-supported Ni catalysts modified with silver for the steam reforming of methane: Effect of Ag on the control of coke formation. Appl Catal A 2007;330: 12–22. https://doi.org/10.1016/j.apcata.2007.06.022.

[74] Gaur S, Haynes DJ, Spivey JJ. Rh, Ni, and Ca substituted pyrochlore catalysts for dry reforming of methane. Appl Catal A 2011;403(1–2):142–51. https://doi.org/10.1016/J.APCATA.2011.06.025.

[75] Hu J, Wang P, Liu P, Cao G, Wang Q, Wei M, et al. In Situ Fabrication of Nano Porous NiO-Capped Ni_3P film as Anode for Li-Ion Battery with Different Lithiation Path and Significantly Enhanced Electrochemical Performance. Electrochim Acta 2016;220:258–66. https://doi.org/10.1016/j.electacta.2016.10.052.

[76] An Z, Zhang J, Pan S. Facile aqueous synthesis and electromagnetic properties of novel 3D urchin-like glass/Ni-$Ni_3P/Co_2P_2O_7$ core/shell/shell composite hollow structures. Dalton Trans 2010;39(14):3378–83. https://doi.org/10.1039/b924449b.

[77] Sheng Q, Li X, Prins R, Liu C, Hao Q, Chen S. Understanding the Reduction of Transition-Metal Phosphates to Transition-Metal Phosphides by Combining Temperature-Programmed Reduction and Infrared Spectroscopy. Angew Chem 2021;60(20):11180–3. https://doi.org/10.1002/anie.v60.2010.1002/anie.202100767.

[78] Yu Z, Yao Y, Wang Y, Li Y, Sun Z, Liu Y-Y, et al. A bifunctional Ni_3P/γ-Al_2O_3 catalyst prepared by electroless plating for the hydrodeoxygenation of phenol. J Catal 2021;396:324–32. https://doi.org/10.1016/j.jcat.2021.02.029.

[79] Guharoy U, Ramirez Reina T, Gu S, Cai Q. Mechanistic insights into selective CO_2 Conversion via RWGS on Transition Metal Phosphides: A DFT Study. J Phys Chem C 2019;123(37):22918–31. https://doi.org/10.1021/acs.jpcc.9b0412210.1021/acs.jpcc.9b04122.s001.

[80] Wang LX, Wang L, Xiao FS. Tuning product selectivity in CO_2 hydrogenation over metal-based catalysts. Chem Sci 2021;12(44):14660–73. https://doi.org/10.1039/d1sc03109k.

[81] Kattel S, Liu P, Chen JG. Tuning Selectivity of CO_2 Hydrogenation Reactions at the Metal/Oxide Interface. J Am Chem Soc 2017;139(29):9739–54. https://doi.org/10.1021/jacs.7b05362.

[82] Popczun EJ, McKone JR, Read CG, Biacchi AJ, Wiltrout AM, Lewis NS, et al. Nanostructured nickel phosphide as an electrocatalyst for the hydrogen evolution reaction. J Am Chem Soc 2013;135(25):9267–70. https://doi.org/10.1021/ja403440e.

[83] Duyar MS, Gallo A, Regli SK, Snider JL, Singh JA, Valle E, et al. Understanding Selectivity in CO_2 Hydrogenation to Methanol for MoP Nanoparticle Catalysts Using In Situ Techniques. Catalysts 2021;11(1):143. https://doi.org/10.3390/catal11010143.